

Counting Stacked Objects from Multi-View Images

Corentin Dumery¹, Noa Etté¹, Jingyi Xu², Aoxiang Fan¹, Ren Li¹, Hieu Le¹, Pascal Fua¹

¹EPFL, ²Stony Brook University

{name.surname}@{epfl.ch, stonybrook.edu}

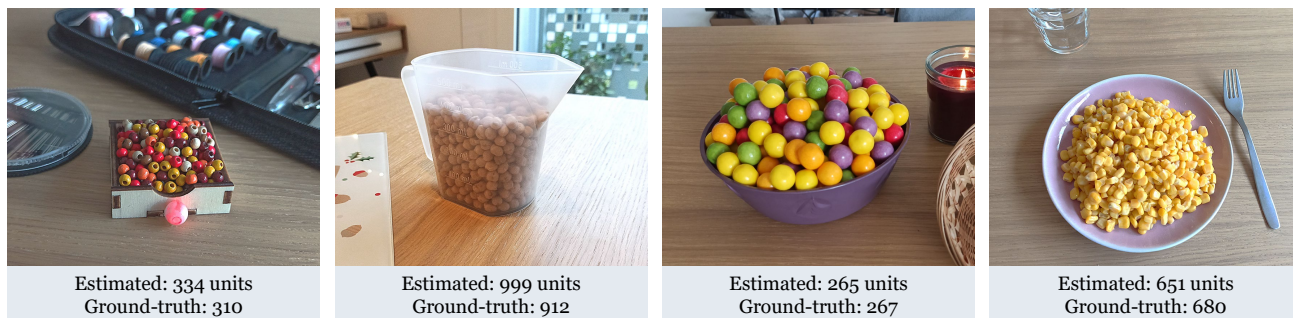


Figure 1. **3D Counting (3DC)**. From multiple views of objects to be counted and their container, we estimate both the total volume they occupy and the fraction of this volume taken up by the objects. Combining these two estimates yields the total number of objects.

Abstract

Visual object counting is a fundamental computer vision task underpinning numerous real-world applications, from cell counting in biomedicine to traffic and wildlife monitoring. However, existing methods struggle to handle the challenge of stacked 3D objects in which most objects are hidden by those above them. To address this important yet underexplored problem, we propose a novel 3D counting approach that decomposes the task into two complementary subproblems - estimating the 3D geometry of the object stack and the occupancy ratio from multi-view images. By combining geometric reconstruction and deep learning-based depth analysis, our method can accurately count identical objects within containers, even when they are irregularly stacked. We validate our 3D Counting pipeline on diverse real-world and large-scale synthetic datasets, which we will release publicly to facilitate further research.

1. Introduction

Visual object counting—the task of quantifying the number of instances in a scene—serves as a fundamental building block for numerous real-world applications and autonomous decision-making systems. This challenging computer vision problem spans diverse domains, from cell

counting in biomedical imaging [28] and traffic [13] or wildlife [1] monitoring. However, existing counting methods [11, 12, 19, 22, 30] can only count visible objects such as apples spread across a table. The problem becomes significantly harder when objects are stacked in 3D configurations, as in Fig. 1. In such scenarios, occlusion poses a fundamental challenge because only a subset of objects remains visible. This requires models to infer the presence and quantity of hidden instances from limited visual cues. This inference task demands architectures that not only can detect visible object features but also reason about occluded objects through contextual understanding. The challenge is further amplified by variations in stacking patterns, object orientations, and irregular arrangements, making traditional counting approaches inadequate. Accurately counting these stacked objects would address significant industrial and agricultural needs, where precise quantification of items—such as products on a pallet or fruits in crates—not only prevents stock and quality errors but also enhances operational efficiency and logistics.

To this end, we address the task of counting stacked objects from multi-view images. In this setting, while some objects are visible from certain viewpoints, most are occluded beneath the stack. The entire stack, however, can be observed from multiple cameras, allowing for a reasonable estimation of its volume and, importantly, the total ob-

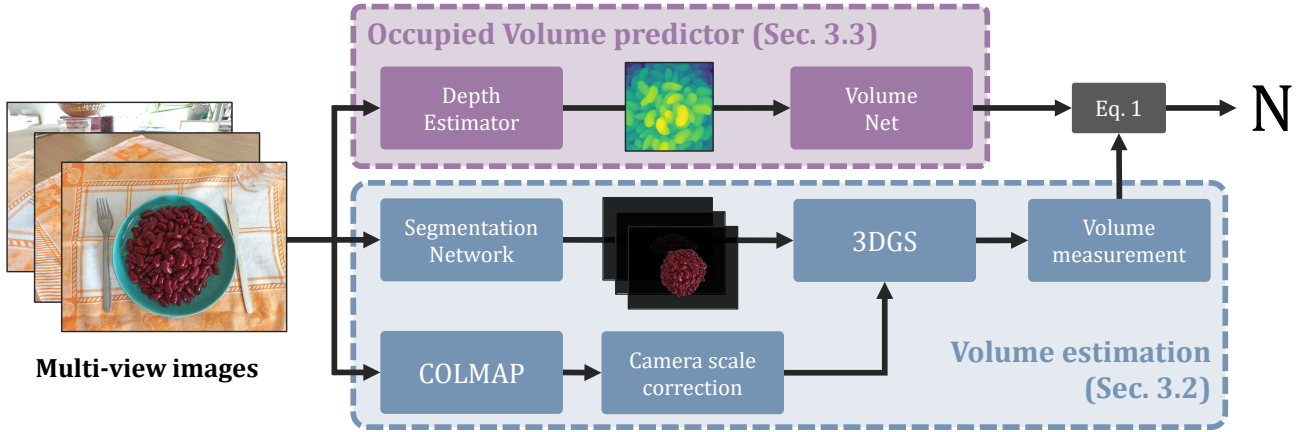


Figure 2. **3DC pipeline.** We decompose the counting task into estimating the volume of the objects to be counted and then estimating the percentage of this volume being used. The first is done on the basis of geometry and second of a depth-map extracted from one of the views.

ject count. We assume the volume of a single object unit is known, which is realistic in scenarios where objects are standardized or belong to a specific class with consistent dimensions, such as packaged goods with minimal variability. We demonstrate that this 3D counting challenge can be solved effectively by decomposing it into two complementary subproblems. As illustrated in Fig. 2, our approach leverages multi-view images of the stack to estimate two key quantities: the 3D geometry of the object stack, and the occupancy ratio of objects within this stack volume. Given the known volume of a single object unit, we compute the total count as the product of the stack volume and occupancy ratio, normalized by the unit volume. This decomposition enables us to solve the 3D counting problem through a combination of geometric reconstruction for volume estimation and deep learning-based depth analysis for occupancy prediction, both of which can be solved efficiently.

We validate our 3D Counting (3DC) approach through extensive experiments on both real-world and synthetic datasets. Our real-world evaluation leverages a diverse collection of scenes depicting diverse objects stacked in containers or still in their original packaging, as illustrated in Fig. 1. To further assess the reliability of 3DC, we also constructed a large-scale synthetic dataset with precisely annotated ground-truth counts. This comprehensive evaluation, along with the public release of our dataset, code, and network weights upon publication, allows for rigorous benchmarking and further advancement of 3D object counting techniques.

Thus, our contributions are:

- A complete pipeline for 3D counting of overlapping, stacked objects, a novel and challenging computer vision task that has not been previously addressed in the literature.

- A network designed to infer the percentage of volume being occupied, which represents a novel idea and forms a key component of the architecture .
- An extensive new 3D Counting Dataset comprising several thousand physically simulated and rendered scenes with precise ground-truth object counts and volume occupancy computed programmatically.
- A complementary real-world validation dataset consisting of 20 scenes captured with multi-view images, accurate camera poses, known unit object volumes, and manually verified total counts.

2. Related work

Counting aims to estimate the number of instances of a specific object category in a scene. Most methods focus on counting visible objects from a single image. A few methods leverage multi-view images to enhance counting accuracy. Our method extends this to a challenging scenario where many of the objects to be counted are occluded, and only multi-view images of the object stack are available. We summarize those related work below.

Single-View Counting. Most recent counting methods focus on single-view scenarios where they train a network specialized in counting a single object-category such as for crowd-counting [3, 10, 23, 25, 27, 29, 35, 36], counting cars [13], or penguins [1]. These methods are applicable in many domains [2] such as counting cells or other anatomical structures in medical imaging [5] or counting trees or building from satellite images [34]. Single-view counting focuses on addressing challenges like scale variation, perspective distortions, and occlusions. To address these, methods often learn robust feature representations [39], employ density map estimation [24], or leverage multi-scale

features [18]. Apart from the traditional setting that specialized in counting a single category, class-agnostic counting [12, 15] enables counting an arbitrary category at test time, given a few image samples of the class [32], a few bounding boxes [19], or just the class name [30]. Like class-agnostic counting methods, our approach is not restricted to specific categories but can generalize to any object type at test time. For the most part, most counting methods only deal with visible objects. The only related attempt to ours is by Jenkins *et al.* [6] that infers counts of occluded objects by incorporating LiDAR data into their setup. However, their approach only handles a specific setup of counting different beverages on shelves for a specific set of categories with known volumes, such as “Coca-Cola 20oz bottle” or “milk carton”, while our method generalizes to diverse scenes, object types, and geometries.

Multi-View Counting. Multi-view counting approaches improve accuracy by combining information across multiple camera views, often projecting feature maps onto a common ground plane to generate precise density maps for crowd counting [37, 38] or segmentation maps of fruits [14]. However, these methods assume that all objects are visible from at least one view and are restricted to a specific class of objects, strongly limiting their applicability in real-world scenarios. In contrast, our method targets the largely unexplored area of counting occluded objects, without any restriction on the nature and shapes of these objects.

3. Method

3DC aims to estimate the total number \mathcal{N} of objects in a container solely from a set of 2D images, which is a challenge even for humans and has not been attempted before to the best of our knowledge.

Our approach is predicated on the idea that, even though we cannot faithfully recover the exact arrangement of all the invisible objects at the bottom of a container, their total number can be inferred by separately estimating their volume in the aggregate, which is a classic vision task, and estimating the object density, which deep learning makes achievable.

After formalizing our approach in Sec. 3.1, we describe our method to performing these two tasks in sections Sec. 3.2 and Sec. 3.3. To train the deep networks we use to estimate density, we created a large synthetic dataset, which we describe in Sec. 3.4 and will make public. Remarkably, as we will see in the results section, even though the networks were trained on this synthetic data, they work effectively on real data as we will see in Sec. 4.

3.1. Problem Statement

Assuming the average volume occupied by a single object is v , and the total volume of the container is \mathcal{V} , it would be tempting to compute the number of objects as $\mathcal{N} = \frac{\mathcal{V}}{v}$. However, this fails to account for gaps between objects. If we consider that the objects are stacked in such a way that only a fraction γ of the volume \mathcal{V} is actually taken up by the objects themselves and that the rest is empty space, then the previous estimate becomes

$$\mathcal{N} = \frac{\gamma\mathcal{V}}{v} \quad (1)$$

Our key insight is that this volume usage rate γ over the whole container can be estimated with high accuracy from the visible elements only. Note that, in general, the density within the container may not be strictly uniform. However, if it is large enough, the variations tend to compensate each other over the whole volume and using an average value is warranted.

Assumptions. To estimate \mathcal{N} from partial visual information, we assume that:

- The objects are stacked uniformly.
- The objects are approximately identical. Their average size v is assumed to be known and does not vary much.
- Some of the objects are partially visible, so that their density γ can be estimated.

These assumptions hold in the real-world scenes of Fig. 1.

Applications These assumptions remain general enough for a wide range of applications across various industries. In warehousing and retail, our proposed setup can be used to automate the inventory process by accurately counting stacked items, reducing the need for manual labor and facilitating restocking. Additionally, in manufacturing, our method can enhance quality control by ensuring that shipped containers include a sufficient number of items. It can also provide 3D scene understanding to autonomous systems for robotic tasks like pick-and-place or sorting. Finally, our algorithm can fill an important need in nutrition tracking to estimate the number of items stacked on a plate, allowing for more accurate calorie estimation based on portion size.

3.2. Volume Estimation

Reconstructing the surface and inferring from it the volume \mathcal{V}_{est} of a set of objects in a container is a well-understood problem. When camera poses are unknown, we use COLMAP [21] to calibrate the images and adjust their scale using a real-world reference measurement. For industrial applications where the camera setup is fixed and known, these calibration and scaling steps are much simpler. Next, we use the SAM2 [20] video segmentation

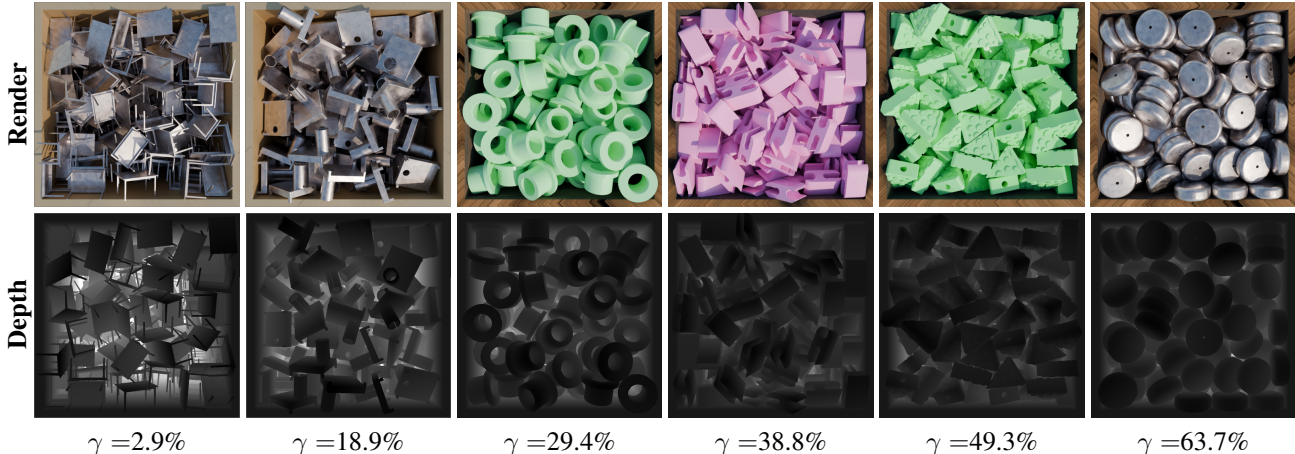


Figure 3. **Dataset samples.** We visualize generated scenes in ascending order of occupied volume ratio, with corresponding depth maps.

model to isolate the container from its surroundings. When the position of the object stack is unknown, the user only needs to select the stack in the first image, and SAM2 will generate masks for all subsequent images. Given these masks, we extract the container and objects by adding the mask as alpha channel. We then optimize 3D Gaussian Splats [7] from these images. Pixels with alpha lower than 1 are supervised with random pixels each iteration, which in effect prevents gaussians in these pixels and ensures our reconstruction covers the container and objects only.

Finally, to estimate the volume from the reconstruction, we consider the point cloud formed by the means of all gaussians in the 3D reconstruction. We first compute the alpha-concave hull [4] of the points, which defines a mesh that closely envelopes the points while allowing some concavities controlled by a parameter α , and thus providing a tighter fit than a convex hull.

Given that the point cloud represents both the container and the objects inside it, this approach effectively isolates the overall shape of both the container and its contents. In a number of cases, the container thickness can be neglected, for example if the stack lies on a flat plane or is inside a thin plastic wrapping. However, if the thickness T of the container cannot be neglected and is specified by the user, we adjust the mesh of the alpha-concave hull to account for the container walls by shifting each vertex inward along its normal by $-T$, thereby refining the estimated volume to represent only the contents. The resulting surface provides us with a good estimate of the volume spanned by the stacked objects.

3.3. Occupied Volume Estimation

Our main intuition is that the volume usage can be very precisely inferred from a depth map computed by a good monocular depth estimator, such as Depth Anything

V2 [31] from a view on which the objects of interest are clearly visible. This view is taken to be the camera that is right above the container, unless the objects are better seen from another angle, in which case it can be arbitrarily set by the user. Optionally, this image is then also cropped to cover only the objects of interest.

We therefore aim to learn a function $\Phi : \mathcal{D} \rightarrow \gamma \in [0, 1]$ that takes as input a depth image and predicts a volume usage γ . Φ learns the relationship between the depth map and the volume usage, including the fact that, if greater depths are visible in the depth map, then the ridges between objects are large and the percentage of volume taken by the object is low. This does not depend on the exact shape of the objects being observed and, should in theory, be applicable to novel inputs with shapes not seen during training. In the results section, we will confirm this to be true in practice.

Network Architecture. To implement Φ , we use a DinoV2 [16] encoder model and train a decoder head to predict the percentage of volume used by the stacked objects. This pretrained encoder extracts rich features from the input depth image, encoding meaningful information and making the task of the decoder easier. While it would be possible to generate a very large amount of data and train a specialized model from scratch, we find that leveraging a foundation model drastically improves convergence speed and reduces the need for a large amount of training data. DinoV2 in particular has shown remarkable performance in monocular depth estimation, which motivates our decision to use it for volume usage prediction.

When designing our decoder head, our goal was to aggregate feature values into a single scalar representing the volume usage as predicted from the whole image. To this end, we use consecutive convolutional layers to gradually decrease the resolution of the features, along with ReLU activations, reducing the encoded feature image to a single

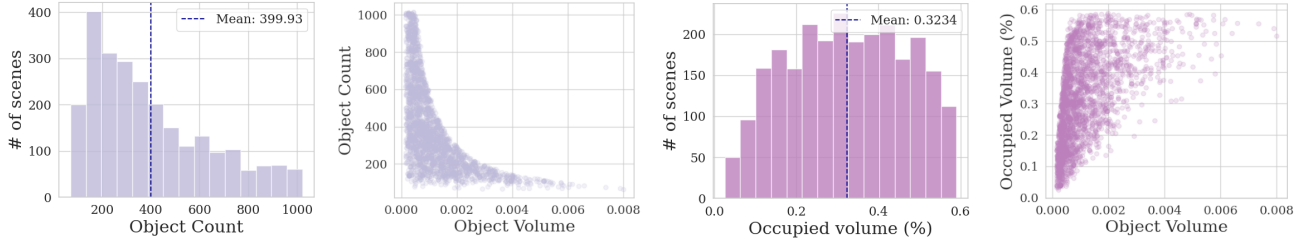


Figure 4. **Dataset statistics.** The histograms represent the distributions of object count and occupied volume, respectively, and each bar plots the number of scenes in a given bin. In scatter plots, each point represents a physically simulated 3D scene. In particular, the occupied volume γ spans a large range between 1% and 65%

pixel with 64 channels, and a final linear layer to predict a single scalar from the output of the last convolutional layer. We refer the reader to our supplementary material for additional details on our network architecture.

Training. We minimize the squared error over the estimated volume usage γ_{est} . To create ground-truth data for supervision purposes, we physically simulate thousands of objects and measure the exact fraction of volume being used by objects in a container in Sec. 3.4. From these simulated 3D scenes, we generate depth maps with Depth Anything V2 [31], and we augment training images using random resized crops and flips. In an ablation study in Sec. 4, we also report the influence of using these estimated depth maps instead of the perfect ground truth depth maps.

3.4. Dataset generation

To train the volume usage estimation network Φ of Sec. 3.3, we require pairs of images and ground-truth volume usage percentage. To this end, we created a novel dataset of physically simulated stacked objects and we measure the exact fraction of volume being used by the objects. We used the ABC dataset [9], that comprises a wide variety of *computer-assisted design* (CAD) models, and we first discard models that are not watertight or that have multiple connected components. We normalized models to fit in a cube of side 0.05. We then generated a virtual 3D scene with a container, and dropped an initial batch of 100 identical objects in that box. We repeated this step until the box is full, that is to say, the union of objects is still intersecting the space above the box even after the physical simulation has converged.

Once the physical simulation was complete, we numerically measured the percentage of volume used as well as the total number of objects in the container. Finally, we render multiple views of the container and objects from several angles to allow 3D reconstruction, as illustrated in Fig. 5. Crucially, this rendering is performed with a ray-tracing engine, and produces realistic images where objects at the bottom of the box appear darker due to ambient occlusion. For each object, a realistic appearance is randomly selected from a



Figure 5. **Multi-view images.** We generate 30 views from arbitrary angles for each of the validation scenes in our synthetic dataset.

range of metallic and plastic materials.

We ran this physical simulation for over 2500 shapes from the ABC dataset, and isolate a subset of 100 shapes to use as a test set. This dataset allows us not only to train Φ , but also to run our complete pipeline on the multi-view images in order to measure the accuracy of our count estimate \mathcal{N}_{est} , as performed in Sec. 4. It also includes ground-truth depth maps, which we employ in an ablation study in our experiments to assess the requirement of accurate depth

| | NAE | SRE | MAE | sMAPE |
|-----------------|-------------|-------------|--------------|--------------|
| BMNet+ [22] | 0.91 | 0.87 | 320.50 | 158.87 |
| SAM[8]+CLIP[17] | 0.73 | 0.61 | 259.22 | 102.77 |
| Ours | 0.22 | 0.09 | 79.48 | 27.65 |

Table 1. **Counting evaluation on synthetic dataset.** We evaluate on our proposed validation dataset of 100 scenes. Since the total count varies widely from 30 to around 1000 units across the simulated scenes, we report normalized metrics.

| | NAE | SRE | MAE | sMAPE |
|-----------------|-------------|-------------|---------------|--------------|
| BMNet+ [22] | 0.98 | 1.00 | 1606.58 | 162.28 |
| SAM[8]+CLIP[17] | 0.95 | 0.99 | 1780.41 | 120.99 |
| Ours | 0.15 | 0.01 | 248.45 | 34.20 |

Table 2. **Counting evaluation on real data.** We capture 20 real scenes comprised of objects in stacks, packages, and various containers for evaluation on real-world applications.

| | MAE | RMSE | sMAPE | R^2 |
|--------------------------|-------------|-------------|--------------|-------------|
| <i>DepthExtrapolated</i> | 0.36 | 0.38 | 77.43 | -6.04 |
| <i>DepthCorrected</i> | 0.10 | 0.12 | 34.80 | 0.28 |
| Mean Estimator | 0.12 | 0.14 | 41.25 | 0.00 |
| Ours | 0.06 | 0.07 | 29.18 | 0.79 |

Table 3. **Occupied volume estimation.** We evaluate our method against two other depth-map based methods, and against the mean estimator which predicts the mean γ of the training set (32.3%).

maps of our method. The resulting dataset encompasses a wide variety of shapes and is illustrated in Fig. 3. We report additional statistics that highlight the diversity of the proposed dataset in Fig. 4.

4. Experiments

We evaluate our method in two ways: measuring the accuracy of 3D counting as a whole and of the volume estimation, in Sec. 4.3 and Sec. 4.2, respectively. These evaluations are performed over two datasets. The first comprises 100 scenes representing physically simulated shapes from the ABC dataset [9]. These scenes were isolated after their generation and were not seen during the training of our occupied volume network. The second is made of 20 real scenes that were captured with a regular smartphone’s RGB camera, and no additional sensor. These captures offer multiple views around stacks of objects in a container, lying flat on a table or still enclosed in their packaging. We measure the ground-truth number of units manually for all scenes below 1000, or infer it from the weight for even larger counts. Some of these captures can be seen in Fig. 1, and more examples are shown in our supplementary material.



Figure 6. **Partial view.** Since our method is designed to be robust to restricted views of the objects to count, it is able to infer an accurate occupied volume ratio from small openings in packaging, such as in the *rice* scene (*Est.* 21649, *G.T.* 20063 (approx.), $\gamma_{est} = 43.1\%$).

4.1. Metrics

We use several metrics to assess the accuracy of object counting and occupied volume estimation. The object counts vary significantly across scenes, ranging from 36 to 20063. Thus, the Mean Absolute Error (MAE)—defined as $MAE = \frac{1}{n} \sum_{i=1}^n |y_i - \hat{y}_i|$, where y_i is the ground truth count and \hat{y}_i is the predicted count for each scene—tends to amplify the importance of scenes with a high counts. To mitigate this, we also report normalized metrics. We use the Normalized Absolute Error (NAE) and Squared Relative Error (SRE), which scale errors relative to the ground truth. The NAE provides a measure of the absolute error normalized by the total ground truth count across scenes, while SRE emphasizes larger errors and penalizes significant deviations in high-count scenes. They are computed as

$$NAE = \frac{\sum_{i=1}^n |y_i - \hat{y}_i|}{\sum_{i=1}^n y_i}, \quad SRE = \frac{\sum_{i=1}^n (y_i - \hat{y}_i)^2}{\sum_{i=1}^n y_i^2}.$$

We also report the Symmetric Mean Absolute Percentage Error (sMAPE), which offers a normalized percentage error. It is defined as

$$sMAPE = \frac{100\%}{n} \sum_{i=1}^n \frac{|y_i - \hat{y}_i|}{(y_i + \hat{y}_i)/2},$$

ensuring that errors are scaled symmetrically between the prediction and ground truth counts. Finally, the coefficient of determination, R^2 , measures the proportion of variance in the ground-truth occupied volume ratio γ explained by our predictions

$$R^2 = 1 - \frac{\sum_{i=1}^n (y_i - \hat{y}_i)^2}{\sum_{i=1}^n (y_i - \bar{y})^2},$$

where \bar{y} is the mean of the ground truth counts. High values of R^2 indicate strong agreement between predictions and ground-truth values.



Figure 7. **Failure cases.** For some highly complex shapes, our method fails to predict an accurate γ_{est} . They are represented in our real dataset, such as the scenes *pasta* (*Est.* 2025, *G.T.* 588, $\gamma_{est} = 23.9\%$) and *pins* (*Est.* 100, *G.T.* 205, $\gamma_{est} = 15.9\%$).

4.2. 3D counting

To the best of our knowledge, there is no previous work on counting from multiple images which does not either implicitly assume all objects to be visible or require additional sensors such as LiDARs. Thus we compare our 3DC approach against BMNet+ [22]. It predicts a density map over all pixels of an image, and the estimated count is then inferred by summing over all pixels. Additionally, we compare against a combination of SAM [8] and CLIP [17], where SAM is used to generate a large number of masks from an input image and CLIP uses a set of negative and positive text prompts to identify masks that represent an object of interest. The final count is then taken to be the number of these masks.

Our method easily outperforms both baselines by a large margin, both on the synthetic (Tab. 1) and the real (Tab. 2) datasets. In Fig. 6, we show that our method can effectively count from a partial view of the objects to be counted.

We further observe that the quality of our results varies little between the synthetic and real datasets, highlighting the generalization ability of our approach. Additionally, we display intermediate stages in Fig. 8, providing further insights into our results. For more visualizations over the complete dataset of real scenes, we refer the reader to our supplementary material.

4.3. Occupied Volume Estimation

We now study the performance of the occupied volume network by itself. There is little work on occupied volume estimation. For this reason, we implement additional baselines to evaluate the effectiveness of our approach, and evaluate them on our proposed synthetic dataset.

Since our hypothesis is that the depth map contains important information to predict this value, we define a first baseline that we will refer to as *DepthExtrapolated*. Given the top view of the container, we compute the maximal depth using a monocular depth estimator and use it to nor-

| | NAE | SRE | MAE | sMAPE |
|---------------------------------------|-------------|-------------|--------------|--------------|
| Ours ($\mathcal{T}-, \mathcal{V}-$) | 0.22 | 0.09 | 79.48 | 27.65 |
| Ours ($\mathcal{T}+, \mathcal{V}-$) | 0.28 | 0.11 | 100.12 | 30.93 |
| Ours ($\mathcal{T}+, \mathcal{V}+$) | 0.31 | 0.12 | 111.04 | 35.92 |

Table 4. **Ablation study on 3D counting.** If ground-truth depth maps are used during training, it is indicated as $\mathcal{T}+$, and $\mathcal{T}-$ otherwise. Similarly, for evaluation purposes if ground-truth depth-maps are used during validation, we indicate it as $\mathcal{V}+$.

| | MAE | RMSE | sMAPE | R^2 |
|---------------------------------------|-------------|-------------|--------------|-------------|
| Ours ($\mathcal{T}-, \mathcal{V}-$) | 0.06 | 0.07 | 29.18 | 0.79 |
| Ours ($\mathcal{T}+, \mathcal{V}-$) | 0.08 | 0.11 | 32.01 | 0.52 |
| Ours ($\mathcal{T}+, \mathcal{V}+$) | 0.10 | 0.13 | 37.35 | 0.32 |

Table 5. **Ablation study on occupied volume estimation.**

malize the depth map. Then, we average the resulting values of the K pixels, yielding the volume fraction estimate

$$\gamma_{est}^{norm} = \frac{1}{K} \sum \frac{d_i}{d_{max}}$$

We observed that this first baseline was biased to predict values lower than expected. We thus defined a second one we dubbed *DepthCorrected*, which uses linear regression to correct γ_{est}^{norm} into a new estimate $\gamma_{est}^{corrected}$. This provides a reasonable baseline that is able to model the observation that depth maps with high variance tend to correspond to low ratios of occupied volume. Finally, we also compare with the mean estimator, that predicts the mean percentage of 32.3% occupied volume for all inputs.

As can be seen in Tab. 3, our method outperforms these baselines by a significant margin. While *DepthCorrected* is more successful than other baselines, showing that the depth information is indeed meaningful for this task, it does not fully predict the occupied volume. We interpret this as a strong clue that the ratio $\frac{d_i}{d_{max}}$ alone is not enough to predict γ , and our proposed network successfully learns to extract meaningful information from the depth maps. We hypothesize that, thanks to the pre-trained foundation model, our volume network is able to capture additional geometric information such as the influence of concavities in the final occupation of volume.

4.4. Ablation study

We also perform additional comparisons to evaluate the sensitivity of our approach to the depth maps produced by the monocular depth estimator. Since our proposed synthetic dataset has ground-truth depth maps both on the training images and the validation images, we perform several experiments.

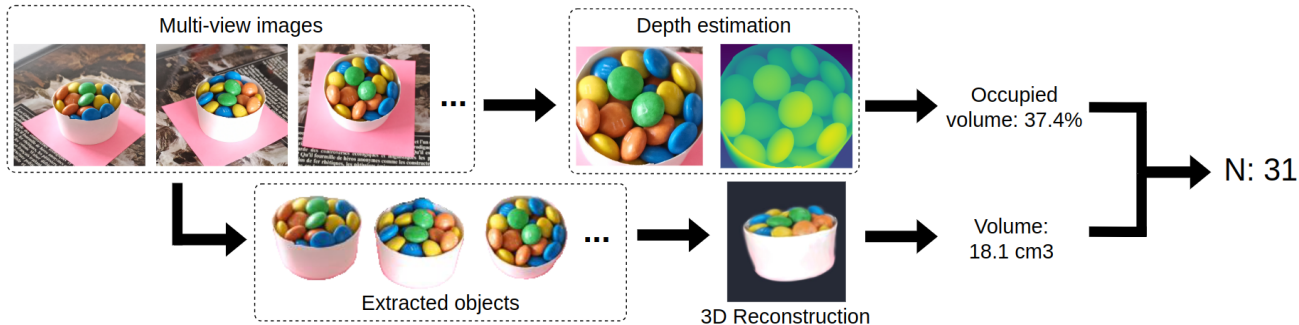


Figure 8. **Intermediate results.** We visualize the outputs of the different stages of our pipeline to provide further insights into their results.

Recall from Sec. 3.3 that, at training time, we use Depth Anything V2 [31] depth maps, a setting we refer to as $\mathcal{T}-$ in Tab. 1 and occupied volume estimation in Tab. 3. Instead, we could use ground-truth depth maps during training, a setting we will refer to as $\mathcal{T}+$. Similarly, for validation purposes, if ground-truth depth-maps are used we designate the method as $\mathcal{V}+$, and $\mathcal{V}-$ otherwise. Thus, the standard configuration of our method is $\mathcal{T}-, \mathcal{V}-$. The others are only used for ablation study purposes.

We report the results in Tab. 1 and occupied volume estimation in Tab. 3. Entirely dropping the ground-truth depth maps and only using the estimated depths proves to be the most successful approach and is the one we use in practice. We hypothesize that this is due to the slight smoothing present in the depth maps produced by Depth Anything v2 [31], which may prevent the model from overfitting to some specific shape features in perfect depth maps of some training samples.

Even though it is trained on synthetic data, this observation further confirms the generalizability of 3DC to real data, since in a practical scenario such as the real data of Tab. 2, ground-truth depth maps are not available.

4.5. Limitations and future work

In Fig. 7, we show failure cases of our method where the shapes of the objects are too complex for our volume occupancy estimator. Future work will focus on refining this estimate to handle highly non-convex and complex shapes. Additionally, and similarly to previous works [12, 15], our method currently expects the user to select the area of interest in at least one of the images. Automating this step as performed in [30] would enhance the ease of use of our method.

Unlike our method, previous works additionally attempt to localize the objects being counted, increasing the interpretability of the results. However, these localizations are often erroneous when objects are stacked together, as illustrated in Fig. 9, greatly limiting their applicability. Thus a

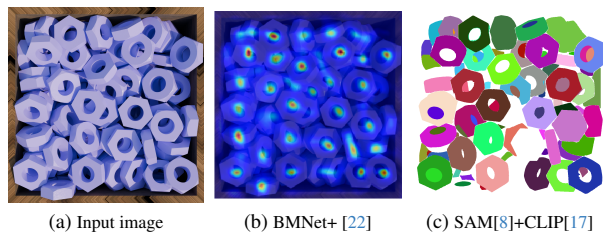


Figure 9. **Instance localization.** Previous methods also produce interpretable results, representing a promising direction for future work.

possible direction for further enhancements lies in integrating a robust localization of visible instances.

5. Conclusion

In this paper, we introduced a novel 3D counting method designed to address the challenges posed by stacks of identical objects, where occlusions and irregular arrangements make accurate counting difficult. By decomposing the counting task into two complementary subproblems—3D geometry estimation and occupancy ratio analysis—we demonstrated that our approach can achieve reliable counts in a wide variety of cases. Through extensive experiments on both real-world and large-scale synthetic datasets, we validated the robustness and accuracy of our method across diverse scenarios, highlighting its potential applications in domains such as logistics, monitoring, and scientific research.

Our pipeline combines geometric reconstruction with deep learning depth analysis, establishing a framework that can generalize well to objects in stacks, packaging, or in a container. By releasing our datasets to the public, we aim to encourage future research and development in 3D counting. In summary, our method represents a significant step forward in visual counting, especially in challenging, stacked 3D settings, and we believe it will inspire new approaches to handling occlusion and spatial complexity in vision counting tasks.

References

- [1] C. Arteta., V. Lempitsky, and A. Zisserman. Counting in the Wild. In *European Conference on Computer Vision*, 2016. 1, 2
- [2] P. Chattopadhyay, R. Vedantam, R.R. Selvaju, D. Batra, and D. Parikh. Counting Everyday Objects in Everyday Scenes. In *Conference on Computer Vision and Pattern Recognition*, 2017. 2
- [3] Z. Cheng, J. Li, Q. Dai, X. Wu, and A. G. Hauptmann. Learning Spatial Awareness to Improve Crowd Counting. In *International Conference on Computer Vision*, 2019. 2
- [4] Herbert Edelsbrunner, David Kirkpatrick, and Raimund Seidel. On the shape of a set of points in the plane. *IEEE Transactions on information theory*, 29(4):551–559, 1983. 4
- [5] Thorsten Falk, Dominic Mai, Robert Bensch, Özgün Çiçek, Ahmed Abdulkadir, Yassine Marrakchi, Anton Böhm, Jan Deubner, Zoe Jäckel, Katharina Seiwald, Alexander Dovzhenko, Olaf Tietz, Cristina Dal Bosco, Sean Walsh, Deniz Saltukoglu, Tuan Leng Tay, Marco Prinz, Klaus Palme, Matias Simons, Ilka Diester, Thomas Brox, and Olaf Ronneberger. U-net: deep learning for cell counting, detection, and morphometry. *Nature Methods*, 16:67 – 70, 2018. 2
- [6] P. Jenkins, Kyle Armstrong, Stephen Nelson, Siddhesh Gotad, J. Stockton Jenkins, W. Warren Wilkey, and Tanner Watts. Countnet3d: A 3d computer vision approach to infer counts of occluded objects. *IEEE Winter Conference on Applications of Computer Vision*, pages 3007–3016, 2023. 3
- [7] B. Kerbl, G. Kopanas, T. Leimkühler, and G. Drettakis. 3d gaussian splatting for real-time radiance field rendering. *ACM Transactions on Graphics*, 42(4), 2023. 4, 1
- [8] A. Kirillov, E. Mintun, N. Ravi, H. Mao, C. Rolland, L. Gustafson, T. Xiao, S. Whitehead, A. C. Berg, W.-Y. Lo, P. Dollár, and R. Girshick. Segment Anything. In *arXiv Preprint*, 2023. 6, 7, 8
- [9] S. Koch, A. Matveev, Z. Jiang, F. Williams, A. Artemov, E. Burnaev, M. Alexa, D. Zorin, and D. Panozzo. ABC: A Big CAD Model Dataset for Geometric Deep Learning. In *Conference on Computer Vision and Pattern Recognition*, pages 9601–9611, 2019. 5, 6
- [10] C. Liu, X. Weng, and Y. Mu. Recurrent Attentive Zooming for Joint Crowd Counting and Precise Localization. In *Conference on Computer Vision and Pattern Recognition*, 2019. 2
- [11] W. Liu, N. Durasov, and P. Fua. Leveraging Self-Supervision for Cross-Domain Crowd Counting. In *Conference on Computer Vision and Pattern Recognition*, 2022. 1
- [12] Erika Lu, Weidi Xie, and Andrew Zisserman. Class-agnostic counting. In *Asian Conference on Computer Vision*, 2018. 1, 3, 8
- [13] Vishal Mandal and Yaw Adu-Gyamfi. Object detection and tracking algorithms for vehicle counting: A comparative analysis. *Journal of Big Data Analytics in Transportation*, 2:251 – 261, 2020. 1, 2
- [14] Anjana K Nellithamaru and George A. Kantor. Rols : Robust object-level slam for grape counting. *Conference on Computer Vision and Pattern Recognition Workshops*, pages 2648–2656, 2019. 3
- [15] Thanh Nguyen, Chau Pham, Khoi Nguyen, and Minh Hoai. Few-shot object counting and detection. In *European Conference on Computer Vision*, pages 348–365. Springer, 2022. 3, 8
- [16] M. Oquab, T. Darcet, T. Moutakanni, H. Vo, M. Szafraniec, V. Khalidov, P. Fernandez, D. Haziza, F. Massa, A. El-Nouby, R. Howes, P. Huang, H. Xu, V. Sharma, S. Li, W. Galuba, M. Rabbat, M. Assran, N. Ballas, G. Synnaeve, I. Misra, H. Jegou, J. Mairal, P. Labatut, A. Joulin, and P. Bojanowski. DINOv2: Learning Robust Visual Features without Supervision. *arXiv Preprint*, 2023. 4, 3
- [17] A. Radford, J. Kim, C. Hallacy, A. Ramesh, G. Goh, S. Agarwal, G. Sastry, A. Askell, P. Mishkin, J. Clark, et al. Learning transferable visual models from natural language supervision. In *International Conference on Machine Learning*. PMLR, 2021. 6, 7, 8
- [18] V. Ranjan, H. Le, and M. Hoai. Iterative Crowd Counting. In *European Conference on Computer Vision*, 2018. 3
- [19] Viresh Ranjan, Udbhav Sharma, Thua Nguyen, and Minh Hoai. Learning to count everything. *Conference on Computer Vision and Pattern Recognition*, pages 3393–3402, 2021. 1, 3
- [20] Nikhila Ravi, Valentin Gabeur, Yuan-Ting Hu, Ronghang Hu, Chaitanya Ryali, Tengyu Ma, Haitham Khedr, Roman Rädle, Chloe Rolland, Laura Gustafson, et al. Sam 2: Segment anything in images and videos. *arXiv preprint arXiv:2408.00714*, 2024. 3
- [21] J.L. Schönberger and J.M. Frahm. Structure-From-Motion Revisited. In *Conference on Computer Vision and Pattern Recognition*, 2016. 3, 1
- [22] Min Shi, Hao Lu, Chen Feng, Chengxin Liu, and Zhiguo Cao. Represent, compare, and learn: A similarity-aware framework for class-agnostic counting. In *Conference on Computer Vision and Pattern Recognition*, 2022. 1, 6, 7, 8
- [23] Z. Shi, P. Mettes, and C. G. M. Snoek. Counting with Focus for Free. In *International Conference on Computer Vision*, 2019. 2
- [24] V.A. Sindagi and V.M. Patel. Generating High-Quality Crowd Density Maps Using Contextual Pyramid CNNs. In *International Conference on Computer Vision*, pages 1879–1888, 2017. 2
- [25] V.A. Sindagi and V.M. Patel. Multi-Level Bottom-Top and Top-Bottom Feature Fusion for Crowd Counting. In *International Conference on Computer Vision*, 2019. 2
- [26] M. Tancik, E. Weber, E. Ng, R. Li, B. Yi, J. Kerr, T. Wang, A. Kristoffersen, J. Austin, K. Salahi, A. Ahuja, D. McAllister, and A. Kanazawa. Nerfstudio: A Modular Framework for Neural Radiance Field Development. In *ACM SIGGRAPH*, 2023. 2, 3
- [27] J. Wan and A. B. Chan. Adaptive Density Map Generation for Crowd Counting. In *International Conference on Computer Vision*, 2019. 2
- [28] Weidi Xie, J. Alison Noble, and Andrew Zisserman. Microscopy cell counting and detection with fully convolutional

- regression networks. *Computer Methods in Biomechanics and Biomedical Engineering: Imaging & Visualization*, 6: 283 – 292, 2018. 1
- [29] C. Xu, K. Qiu, J. Fu, S. Bai, Y. Xu, and X. Bai. Learn to Scale: Generating Multipolar Normalized Density Maps for Crowd Counting. In *International Conference on Computer Vision*, 2019. 2
- [30] Jingyi Xu, Hieu Le, Vu Nguyen, Viresh Ranjan, and Dimitris Samaras. Zero-shot object counting. *Conference on Computer Vision and Pattern Recognition*, pages 15548–15557, 2023. 1, 3, 8
- [31] Lihe Yang, Bingyi Kang, Zilong Huang, Zhen Zhao, Xiaogang Xu, Jiashi Feng, and Hengshuang Zhao. Depth anything v2. *arXiv preprint arXiv:2406.09414*, 2024. 4, 5, 8, 3
- [32] Shuo Yang, Hung-Ting Su, Winston H. Hsu, and Wen-Chin Chen. Class-agnostic few-shot object counting. *2021 IEEE Winter Conference on Applications of Computer Vision (WACV)*, pages 869–877, 2021. 3
- [33] Vickie Ye, Ruilong Li, Justin Kerr, Matias Turkulainen, Brent Yi, Zhuoyang Pan, Otto Seiskari, Jianbo Ye, Jeffrey Hu, Matthew Tancik, and Angjoo Kanazawa. gsplat: An open-source library for Gaussian splatting. *arXiv preprint arXiv:2409.06765*, 2024. 3
- [34] Jun Yi, Zhilong Shen, Fan Chen, Yiheng Zhao, Shan Xiao, and Wei Zhou. A lightweight multiscale feature fusion network for remote sensing object counting. *IEEE Transactions on Geoscience and Remote Sensing*, 61:1–13, 2023. 2
- [35] A. Zhang, J. Shen, Z. Xiao, F. Zhu, X. Zhen, X. Cao, and L. Shao. Relational Attention Network for Crowd Counting. In *International Conference on Computer Vision*, 2019. 2
- [36] A. Zhang, L. Yue, J. Shen, F. Zhu, X. Zhen, X. Cao, and L. Shao. Attentional Neural Fields for Crowd Counting. In *International Conference on Computer Vision*, 2019. 2
- [37] Q. Zhang and A.B. Chan. 3D Crowd Counting via Multi-View Fusion with 3D Gaussian Kernels. In *AAAI Conference on Artificial Intelligence*, 2020. 3
- [38] Qi Zhang and Antoni B. Chan. Wide-area crowd counting: Multi-view fusion networks for counting in large scenes. *International Journal of Computer Vision*, 130:1938 – 1960, 2020. 3
- [39] Y. Zhang, D. Zhou, S. Chen, S. Gao, and Y. Ma. Single-Image Crowd Counting via Multi-Column Convolutional Neural Network. In *Conference on Computer Vision and Pattern Recognition*, pages 589–597, 2016. 2

Counting Stacked Objects from Multi-View Images

Supplementary Material

6. Dataset Details

6.1. 3DC-Real dataset.

We capture 20 real scenes where the objects to count can be any stack of items that are at least partially visible. This includes stacked objects on a table or on the floor, objects in containers such as bowls or boxes, or objects still in their packaging. In Fig. 10, we display all the scenes that were not already presented in our main submission.

Cameras. We use a regular RGB smartphone camera to capture 30-60 pictures of the scene from various angles, forming a semisphere surrounding the objects and their container. These images are downscaled to approximately 600 pixels wide to reduce memory usage and facilitate the processing with COLMAP [21]. Additionally, we take a measurement of an arbitrary object within the scene, allowing us to scale the camera measurements and align the unit distance of the scene with a meter in the real world.

Initially, we experimented with triangulation methods using two pairs of corresponding points across images. This would enable the calculation of a 3D distance and allow us to scale the scene. However, this approach proved unstable, as small inaccuracies in point matching led to significant variations in the scaling. Instead, we reconstructed the 3D scene with 3DGS [7] and measured the 3D distance directly within the reconstruction. This measurement allows us to rescale the scene to match the reference measurement. Note that the 3D point cloud generated by COLMAP [21], which is used as an initialization by 3DGS, is also scaled accordingly.

Unit volume. For each scene, we require the unit volume of the object being counted. For many common food items, such as kidney beans or corn, this information is readily available online. For other scenes, the volume can be approximated, for example in the case of the beads in Fig. 1, by subtracting the volume of a cylinder from that of a sphere. Alternatively, we determine the volume by measuring the number of units needed to displace 100 milliliters of water.

Pre and Post-processing. Using this method, we capture 20 scenes consisting of various items in different environments. The scenes vary in complexity, from simple quasi-spherical objects in containers to more challenging configurations, such as complicated shapes still in packaging (e.g., in the *pasta* scene). Occasionally, we reuse items for a second scene in a different setting, such as by removing objects from their packaging or changing containers.



Figure 10. **Additional dataset samples.** We report the results on all real scenes that are not already present in our main submission.

6.2. 3DC-Synthetic Dataset.

To generate our large-scale synthetic dataset, we utilize Blender, a free and open-source 3D creation suite that supports Python scripting. This allows us to implement a fully automated generation pipeline, which is mainly composed of two steps: simulation and rendering.

Simulation. We drop batches of objects, arranged in a $4 \times 4 \times 5$ grid, into a box positioned at $(0, 0, 0.5)$. The box has a side length of 1 and a thickness of 0.04. Once the simulation converges, we check if the union of the objects intersects with an invisible cube placed directly on top of the box. If an intersection occurs, the simulation stops, and objects outside the box are deleted. If no intersection is detected, a new batch of objects is added, and the simulation is performed again.

We use the convex hull to compute collision between ob-

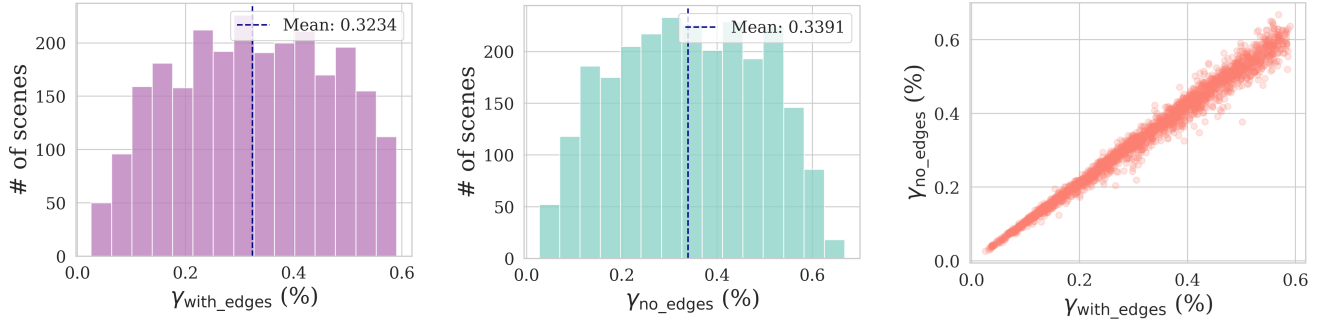


Figure 11. **Border effects.** Measuring the ground-truth γ over the complete box or over only a smaller section makes little difference, indicating that our assumption of uniform γ across the volume is justified.

jects. Ideally, we would use the triangle mesh itself, however this becomes far too costly when physically simulating thousands of shapes with tens of thousands of triangles. We experimented with using convex hulls first, and then refining with additional frames using the triangle mesh, but this turned out to still be extremely costly and computationally very unstable, leading to objects being ejected outside the box due to the change in collision computation.

Rendering. For rendering, we use a texture randomly sampled from 3 possibilities for the box, five textures for the ground, and a random material for each model chosen from one of the following: a realistic grey metal texture, a red metallic texture, or a plastic material with a randomly selected color.

We always render the first view directly above the box, looking downwards, which we call the *nadir* view. For the validation dataset, we also generate 29 additional views on the unit sphere, each observing the box from different angles. The rendering is performed using Blender’s Cycles rendering engine. Additionally, we generate ground-truth depth maps and masks that separate the ground, box, and objects in the images.

Pre and Post-processing. In addition to the simulation and rendering steps, we perform pre-processing to filter out unsuitable meshes, such as those with multiple connected components or excessive size. Since the physical simulation can sometimes be unstable or fail, we also remove a small fraction of results in post-processing. This includes cases where the unit volume is too small or where too few objects remain in the box in the final frame.

Finally, we export the calibrated camera parameters in a format compatible with nerfstudio [26]. Since these cameras are not produced by COLMAP, they do not include a 3D point cloud that 3DGS can use as initialization. This poses a challenge, as a fully random initialization may generate distant Gaussian points outside the cameras’ range, which are not removed and interfere with the volume esti-

mation. To address this, we generate a set of 100 grey points within the unit cube, centered at $(0, 0, 0.5)$. This simple initialization proves sufficient to quickly produce a faithful 3D reconstruction and resolves the aforementioned issue.

7. Additional Discussion on Border Effects

In our work, we assume that the occupied volume ratio, γ , is approximately uniform throughout the container. This assumption generally holds as the number of stacked objects increases. However, it neglects the influence of container borders, where objects tend to occupy less volume due to the boundary.

To quantitatively evaluate the impact of border effects and verify the validity of our uniform γ assumption, we analyze the ground-truth volume ratio in two distinct ways using our large-scale synthetic dataset. First, we compute $\gamma_{\text{with_edges}}$ for the entire unit box, as described in the main paper. Additionally, we compute $\gamma_{\text{no_edges}}$ by measuring the volume ratio in a smaller sub-box of side length 0.5, centered within the unit box. Intuitively, the difference between $\gamma_{\text{with_edges}}$ and $\gamma_{\text{no_edges}}$ reflects the influence of border effects, allowing us to evaluate whether this assumption is justifiable.

Figure 11 presents two histograms comparing the distributions of $\gamma_{\text{with_edges}}$ and $\gamma_{\text{no_edges}}$. The results indicate that both metrics follow highly similar distributions, with their mean values differing by less than 5%. Notably, the mean value of $\gamma_{\text{no_edges}}$ is slightly higher than that of $\gamma_{\text{with_edges}}$, consistent with the intuition that density decreases near borders.

To further investigate the relationship between these two values, we provide a scatter plot of $\gamma_{\text{with_edges}}$ versus $\gamma_{\text{no_edges}}$ in Fig. 11. The plot demonstrates a strong correlation between the two measures, particularly for objects with small volume ratios. For objects with high values of both $\gamma_{\text{with_edges}}$ and $\gamma_{\text{no_edges}}$, minor discrepancies are observed. These differences can be attributed to the relatively large size of these objects compared to the measurement box,

which introduces noise in the estimation of γ .

Overall, these analyses confirm that $\gamma_{\text{with_edges}}$ and $\gamma_{\text{no_edges}}$ are highly consistent and can be used interchangeably without significant loss of accuracy. In our experiments, we rely on $\gamma_{\text{with_edges}}$ to train our occupied volume estimation network.

8. Implementation details

We use the nerfstudio library [26] for 3D reconstruction, specifically the *splatfacto* method built on top of the gsplat library [33]. A combination of trimesh and the alphashape python library to compute alpha concave hulls and measure their volume. We thank the contributors of all the aforementioned libraries.

Our pipeline also uses pretrained models for depth estimation and mask generation. We employ the *vitl* model from Depth Anything v2 [31] for depth estimation and the *sam2.1_hiera_large* model from SAM2 [20] for mask generation. These state-of-the-art models ensure high-quality and robust outputs across diverse scenes.

The dataset is generated using CPUs only, greatly reducing its production cost and environmental impact. Other operations are fairly light and performed locally on a 4080 Mobile GPU, taking up only a few gigabytes of VRAM and being completed in a couple minutes.

9. Architecture details

Our architecture utilizes a DinoV2 [16] encoder model that produces pixel-aligned features. Since DinoV2 downscales the input image by 14, we feed it an image of size 448 x 448 to produce a 32 x 32 x 768 feature image. Specifically, we use the pretrained weights of the *dinov2_vitb14* model and freeze them during all subsequent learning.

To predict a scalar value from the $32 \times 32 \times 768$ feature image produced by DinoV2, we employ a series of convolutional layers to progressively reduce both the spatial dimensions and the number of channels. The convolutional layers successively reduce the channel dimension from the initial 768 down to 512, 256, 128, and finally 64. Concurrently, the spatial dimensions of the feature map are reduced from 32×32 to 16×16 , 8×8 , 4×4 , and ultimately 2×2 .

Following this, an adaptive average pooling layer compresses the spatial dimensions to a single pixel while preserving the 64-channel depth. The resulting $1 \times 1 \times 64$ tensor is passed through a fully connected linear layer to map it to a scalar output. Finally, a sigmoid activation function is applied to produce the final prediction in the $[0, 1]$ range.